Structures 56 (2023) 104900

Contents lists available at ScienceDirect

Structures

journal homepage: www.elsevier.com/locate/structures

The effects of geometric and metallurgical constraints on ultra-high strength steel weldments

Riku Neuvonen [a,*], Teemu Peltoniemi [b], Tuomas Skriko [c], Mehran Ghafouri [a], Mohsen Amraei [d], Antti Ahola [a], Timo Björk [a]

[a] Laboratory of Steel Structures, Lappeenranta-Lahti University of Technology LUT, PL20, 53851 Lappeenranta, Finland
[b] Ponsse Plc, Ponssentie 22, 74200 Vieremä, Finland
[c] Laboratory of Welding Technology, Lappeenranta-Lahti University of Technology LUT, PL20, 53851 Lappeenranta, Finland
[d] University of Turku, Joukahausenkatu 3-5, 20520 Turku, Finland

ARTICLE INFO

Keywords:
Ultra-high strength steel
Welding
Ultimate capacity
Static strength
HAZ softening
Constraint effects

ABSTRACT

The effect of geometric and metallurgical constraints on the ultimate capacity of weldments manufactured from direct-quenched (DQ) ultra-high strength steel (UHSS) is studied using numerical calculations. In addition, experimental tests are conducted to prove the phenomena in practice. DQ steels behave differently under static loading, especially their weldments, compared to the same-strength class steels, which are manufactured using different alloying and fabrication techniques. In these steels welding generates a distinct softened region at the heat-affected zone (HAZ), which, in certain conditions, can influence the ultimate load-carrying and elongation capacity of the weldment. Metallurgical constraints can form in welds where the soft zone is adjacent to zones with higher strength. Moreover, the current study shows that not only metallurgical constraints, but also geometric ones, can strengthen weldments depending on the joint type. Removing the geometrical constraints from weldments slightly reduces the ultimate load-carrying capacity, while a remarkable reduction is seen in the elongation capacity of the joint. Numerical analysis conducted for non-load carrying X-joints indicates that as the width of the soft zone increases, the effect of the geometric constraint diminishes. Thus, it appears that geometric constraints can, in certain cases, prevent the detrimental effect of strain localization from occurring in the soft regions in at the HAZ. This mechanism seems to increase both the ultimate load-carrying capacity and ultimate elongation of weldments.

1. Introduction

Currently humanity's use of resources exceeds the sustainable limits of our planet. According to Aksel and Eren [1], the construction industry uses a remarkable share of global resources. One way to minimize the environmental effect of any new building or machine is to use less material in an effective manner [1]. Use of novel ultra-high strength steels (UHSS) can provide designers with an opportunity to use less material without compromising the strength of the building. A cost-effective way to produce UHSS is to use the direct quenching (DQ) method [2,3]. According to previous studies [3-5], the mechanical properties of DQ UHSSs differ from those of steels produced using conventional quenching and tempering (QT). Thus, it is necessary to distinguish and study these steels separately.

Current European standards concerning the design of steel structures are limited to steel grade S700 [6]. On the other hand, the standard for mobile cranes [7] covers the use of UHSS, for example grades S890, S960, and S1100. It is important to gain more knowledge of the behavior of UHSS and DQ UHSSs to validate these steels to international standards. This might increase the use of both steel types, hence decreasing the total amount of steel used in buildings, machines, and limiting environmental effects.

Porter [8] has shown that DQ UHSSs are more susceptible to softening at the heat-affected zone (HAZ) than QT UHSSs (see Fig. 1). Some recent studies have raised concerns about the effect of this soft HAZ on the static capacity of weldments manufactured from DQ UHSS [9,10]. According to such research, in certain conditions, the ultimate capacity, including both load-carrying and deformation capacities, of welded joints can decrease compared to the base material.

Many researchers have investigated the effect of metallurgical constraints on the ultimate capacity of steels. Amraei et al., [11] and Ran

* Corresponding author.
E-mail address: riku.neuvonen@lut.fi (R. Neuvonen).

https://doi.org/10.1016/j.istruc.2023.104900
Received 11 September 2022; Received in revised form 12 April 2023; Accepted 14 July 2023
Available online 19 July 2023

Nomenclature

symbols and abbreviations

f_y	yield strength
f_u	ultimate tensile strength
A_t	elongation at fracture
$t_{8/5}$	cooling time between 800 and 500 °C
HV_5	Vickers hardness
$f_{y,HV5}$	yield strength calculated from hardness measurement results
$f_{u,HV5}$	ultimate tensile strength calculated from hardness measurement results
$f_{y,FEM}$	yield strength in the material model
ε_D	equivalent plastic strain at damage initiation
D	damage parameter
u_f	equivalent plastic displacement at fracture
E_t	tangent modulus
E	Youngs modulus
V	Poisons ratio
t_b	thickness of base plate
UHSS	ultra-high strength steel
DQ	direct quenching
QT	quenching and tempering
HAZ	heat affected zone
FE	finite element
GMAW	gas metal arc welding
BM	base metal
WM	weld metal
B	experimental butt weld specimen
X	experimental non-load carrying X-joint specimen
w_{HAZ}	width of HM zone in models
w_{reinf}	width of the weld bead in specimen B
h_{reinf}	height of the weld bead
h_{root}	height of the weld root
a	throat thickness
g	air gap in X-joint
t_a	thickness of the attached plate
h_a	height of the attached plate in X-joint
w_a	width of the arrow plate
w_b	width of the base plate
α	angle of the arrow plate
F_{max}	maximum force measured in experiments and models
A_{nom}	nominal cross-section of the specimens
f_{ynom}	nominal yield strength of the base material
A	experimental arrow plate specimen
AW	specimen in as welded condition
GF	specimen with geometrical constraint removed
CGHAZ	coarse grained heat affected zone
FGHAZ	fine grained heat affected zone
SCHAZ	subcritical heat affected zone
DIC	digital image correlation
BF	numerical model of butt weld
XF	numerical model of non-load carrying X-joint
AF	numerical model of arrow plate joint

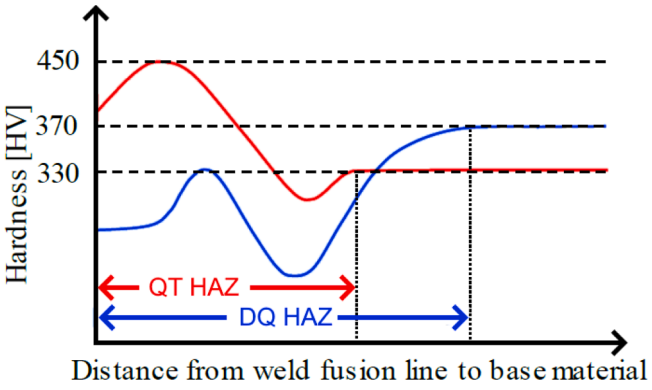

Fig. 1. Illustrative presentation of hardness distributions from HAZs of QT S960 and DQ S960 steels. (Modified from [8,9]).

et al., [12] note that the relative dimensions of the base plate and the thickness and width of HAZ have a clear effect on the strength and deformation capacity of a joint containing a zone of weaker material. Rodrigues et al., [13] and Sun et al., [14] note that the intensity of the strengthening effect also depends on the mismatch degree and hardening parameters of adjacent materials. In addition to the numerical values of ultimate capacity, metallurgical constraints can influence the fracture initiation location. This phenomenon has been observed by Björk et al., [10]. Neuvonen et al., [15] conducted a detailed study concerning metallurgical constraints and numerical evaluation of the ultimate capacity and fracture estimation on tensile specimens when such constraints are present. Their study shows that metallurgical constraints influence both the elongation and ultimate load-carrying capacity as well as the location of fracture initiation of weldments. In addition, it was noted when suitable material models and parameters are used, numerical methods can be employed to investigate the decrease of deformation capacity as well as failure location.

In this study, the effects of both geometric and metallurgical constraints on the ultimate capacity of three different weldments are investigated using finite element (FE) models and experimental tensile tests. In order to vary the degree of geometric and metallurgical constraints in the models, certain aspects of the geometry of the models were varied. The basic setup of the models was based on six different weldments manufactured using gas metal arc welding (GMAW) for the study. The six experimental specimens consisted of two butt welded joints, two non-load carrying X-joints, and two arrow plate reinforcement joints.

Tensile tests were conducted to compare the joint's strength and their deformation capacity. The applicability of the simplified models was verified by comparing the experimental and numerical results. The FE results correlated reasonably well with the experimental results.

Temperature distribution due to welding, which is responsible for the microstructural changes, were obtained using FE thermal analysis. Three-dimensional FE models were developed and the heat from the welding torch was applied as a volumetric heat flux. Upon the thermal analysis of the X-joints, nodal temperatures, and subsequently, cooling times were captured, and the width of HAZ in each case was determined.

The numerical calculations and experimental results indicated that both metallurgical and geometric constraints affect the ultimate load-carrying capacity of the weldments in both butt welds and non-load carrying X-joints. In the case of the arrow-shaped reinforcement plate, the ultimate load carrying capacity was not affected by the removal of the attachment. In all cases, the ultimate deformation capacity was reduced when the geometric constraint was not present.

2. Methods

2.1. Experimental procedure

In this study, two butt welded, two non-load carrying X-joint, and two arrow plate specimens, presented in Fig. 2, were manufactured from

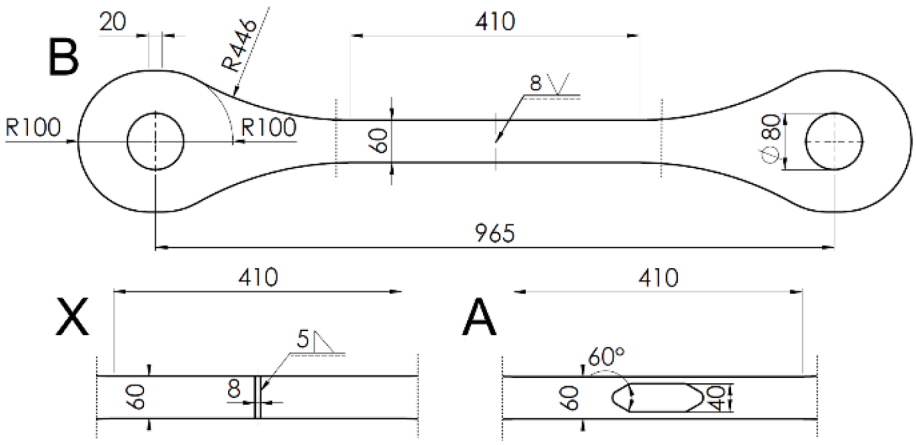

Fig. 2. Geometry of the specimens (letters B, X and A refer to the joint type).

Table 1
Chemical composition of the studied materials.

Material	C	Si	Mn	P	S	Al	N	Cu	Cr	Ni	Mo	Sn	Fe
	[%]	[%]	[%]	[%]	[%]	[%]	[%]	[%]	[%]	[%]	[%]	[%]	
S960MC	0.097	0.2	1.08	0.008	0.001	0.033	0.006	0.015	1.1	0.08	0.129	0.004	bal.
G 89 5 M21 Mn4Ni2.5CrMo	0.12	0.8	1.9	–	–	–	–	–	0.45	2.35	0.55	–	bal.

Table 2
Mechanical properties of the studied materials.

Material	f_y [MPa]	f_u [MPa]	A_t [%]	Charpy-V [kJ]
S960MC	1061	1161	11	64 (-40 °C)
G 89 5 M21 Mn4Ni2.5CrMo	930	980	14	47 (-50 °C)

Table 3
Welding parameters.

Specimen/ Pass	Current [A]	Voltage [V]	Travel speed [mm/s]	Wire feed [m/ min]	Heat input [kJ/ mm]	Cooling time $t_{8\text{-}5}$ [s]
B/1	249	26.1	9.35	13.4	0.60	2.7
B/2	258	26.1	9.97	16.3	0.58	2.6
X	256	26.6	5.62	15.5	1.03	3.5
A/Head	202	26.6	9.00	10.0	0.42	1.4
A/Side	202	26.6	8.00	10.0	0.48	1.6

an 8-mm-thick sheet of DQ UHSS S960MC; hereafter, the specimens are referred to as B, X, and A, respectively. The chemical composition and mechanical properties according to the material certificate are presented in Table 1 and Table 2, respectively. In Table 2 the values for base metal (BM, S960MC) are extracted from the material certificate delivered by the material supplier, and the values for the weld metal (WM, G 89 5 M21) are the nominal values. One of each type of specimens was kept in as-welded condition, hereafter referred to as AW. Another of the specimen pairs was machined to remove the geometric constraint introduced by the weld bead and attached plate. These specimens are referred to as GF. The geometry of the specimens is presented in Fig. 2.

The specimens were welded using GMAW in laboratory conditions. A matching filler wire G 89 5 M21 Mn4Ni2.5CrM, brand name Union X96, with a 1-mm diameter, was used in all welds. The nominal chemical composition and mechanical properties of the filler wire are presented in Table 1 and Table 2, respectively. Specimen set B was in a flat position to a 50° V-groove, using two passes. Set X and A specimens were welded with one pass in a horizontal position. To achieve a good weld quality,

Table 4
Measured weld dimensions.

Specimen	Measured throat thickness [mm]
B_{AW}	10.7
B_{GF}	10.7
X_{AW}	5.3
X_{GF}	5.2
A_{AW}	3.9
A_{GF}	3.8

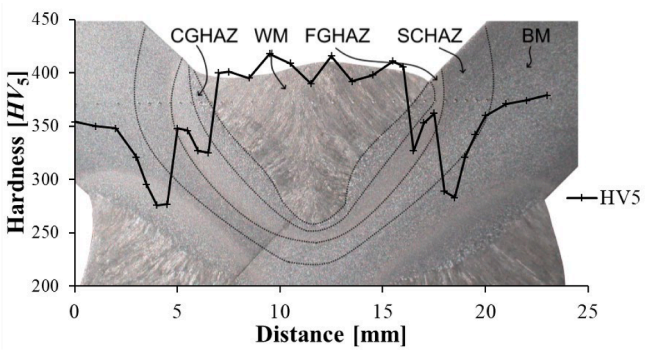

Fig. 3. Macrograph of specimen X_{AW}.

the sides and heads of the set A specimens were welded with slightly different parameters.

The applied welding parameters were adjusted based on the throat and plate thicknesses presented in the drawings (see Fig. 2). The welding parameters are presented in Table 3. The cooling times presented in Table 3, $t8_{/5,}$ were calculated from the heat input using method presented in [16].

In this research, the main point was not to study the effect of different welding parameters on the properties and behavior of different welded connections but to compare different structural cases in question and thus, a certain weld sizes and welding parameters were set.

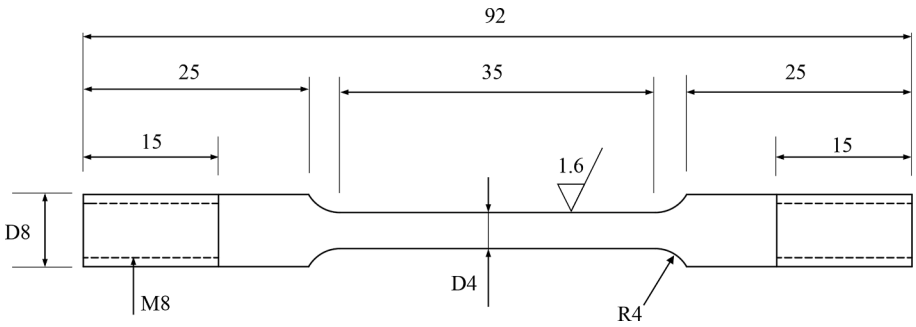

Fig. 4. Schematic of the cylindrical specimen used in tensile tests (Dimensions in mm).

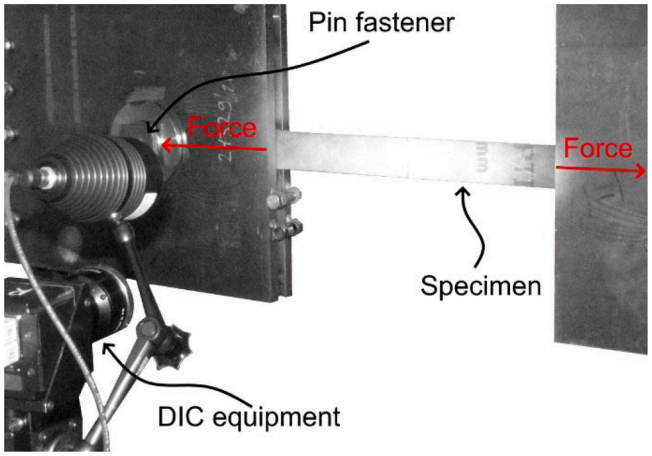

Fig. 5. Tensile test setup with DIC equipment.

The throat thickness of welds was measured using a laser scanning device. The measured results are presented in Table 4 and which were later used in the generation of FE models. The quality of the welds and dimensions of the HAZ region were evaluated from macrographs of polished cross sections. Macrographs of the specimen $X_{AW,}$ with hardness distribution and presentations of different HAZ regions, are presented in Fig. 3. The softening of HAZ described by Porter [8] is clearly visible in the hardness distribution.

In order to obtain the stress–strain curve for the base material, cylindrical specimens were machined from the base material to meet the requirements of ASTM E8M [17], as shown in Fig. 4. As-welded specimen was extracted from a double-V groove butt-welded workpiece which was laser cut, and then machined according to the specifications of ASTM E8M.

Strain-controlled tensile tests were carried out with a constant strain rate of 1×10^{-4} s^{-1} on a Zwick/Roell Z100 testing machine [18].

Tensile tests for specimens in Fig. 2 were conducted for the specimens described above, using a 5 MN servo-hydraulic test rig with displacement control. The test setup is presented in Fig. 5. In addition to a force and displacement sensor of the test rig, digital image correlation (DIC) 3D strain measurement equipment, known as ARAMIS, was used to record the displacement data during the experiment. Two cameras of the DIC system were set-up and the system were calibrated prior testing according to manufacturers recommendations.

One of each type of specimens was tested in the as-welded condition, in which the weld bead or attached plate generated a geometric constraint to strengthen the weldment. For the second specimen, the reinforcement was removed by machining the specimens, thus removing the geometric constraint but leaving the softened HAZ to the specimens. The material with higher strength adjacent to the softened HAZ with lower strength creates a metallurgical constraint to strengthen the soft zone. Thus, in the first specimens, both metallurgical and geometric constraints were present while in the second ones, only the metallurgical constraint was present.

Since there is a clear soft region with adjacent harder regions in the joint (see Fig. 3), a metallurgical constraint, as described in the introduction section, is present in the specimen. According to the literature [11,12,13,14], realistic material properties should be used in the HAZ region to investigate the constraint effect.

The metallurgy of any weld, and especially at the HAZ in DQ UHSS, is very complex. The HAZ itself undergoes various heating and cooling cycles, depending on the distance from the weld fusion line, which result in the formation of various steels. This region includes four different zones at which the pick temperature ranges approximately between 670 and 890 °C for the studied DQ UHSS in this paper [19]. At the soft zone, the temperature is not high enough to fully austenitize the microstructure, and due to the slow cooling rate, the partially austenitized material does not transform into martensite and bainite. Thus, the final microstructure at this region includes a considerable amount of tempered martensite which results in deteriorated mechanical properties compared to both the base material, and the weld fusion zone [19].

The main aim of this study is to demonstrate the constraint effect on the overall behavior of the joint using numerical calculations, not to describe the tensile properties of HAZ in detail. Thus, a simplification was made whereby only three distinct material zones were used in the calculations, namely BM, WM, and HAZ. The authors acknowledge that a more detailed model including different HAZ regions could yield more accurate results. However, as it will be further discussed in the results section, the use of a single HAZ, as used in other studies [12-14], is enough to gain reasonable agreement between experimental and numerical results.

To incorporate the mechanical properties of the softened HAZ into

Table 5
Hardness measurements and calculated yield and tensile strengths of X_{AW} and X_{GF} specimens.

	X_{AW}			X_{GF}			Average		
	HV_5	$f_{y,HV5}$	$f_{u,HV5}$	HV_5	$f_{y,HV5}$	$f_{u,HV5}$	HV_5	$f_{y,HV5}$	$f_{u,HV5}$
WM	381	1005	1323	403	1068	1405	397	1037	1364
CGHAZ	314	812	1073	324	841	1110	319	827	1092
FGHAZ	347	907	1196	352	922	1215	523	915	1206
SCHAZ	277	706	935	281	718	950	418	712	943
BM	342	893	1177	362	950	1252	352	922	1215

Table 6
Goldak's heat source parameters.

Parameter	a(mm)	b_f(mm)	b_r(mm)	c(mm)	f_f	f_r
Value	10	4	10	11	0.57	1.43

the finite element modeling, the correlation between the Vickers hardness and strength (both yield and ultimate) was utilized. Even though there are various formulae for these approximations, the proposed model by Pavlina and Van Tyne [20] is demonstrated to be a good estimation for steels with complex microstructures such as the DQ UHSS in this study [19]. The formulas (1) and (2) presented in [20] were used to convert the hardness measurement results to strength values. These strength values were used as a first estimate to generate material models for FEM. The hardness values and calculated yield and tensile strengths of both set X specimens are presented in Table 5.

$$f_y = -90.7 + 2.876H_v \tag{1}$$

$$f_u = -99.8 + 3.734H_v \tag{2}$$

2.2. FE simulation of welding and thermal analysis

Transient thermal field due to a moving heat source during welding is defined based on constitutive heat conduction equation:

$$\rho(T)c_p(T)\frac{\partial T}{\partial t} = \frac{\partial}{\partial x}\left(k(T)\frac{\partial T}{\partial x}\right) + \frac{\partial}{\partial y}\left(k(T)\frac{\partial T}{\partial y}\right) + \frac{\partial}{\partial z}\left(k(T)\frac{\partial T}{\partial z}\right) + \dot{Q}_v \tag{3}$$

where $\rho(T)$, $c_p(T)$, and $k(T)$ are temperature-dependent density, specific heat, and conductivity, respectively. $\dot{Q}_v$ is volumetric heat source density and t represents time. Arc energy transferred from the welding torch to the base and weld metals during welding was considered as a volumetric heat flux based on the double ellipsoidal heat source model proposed by Goldak et. al [21] with two heat flux distributions, one for the front half (Eq. (4)) and the other for the rear half (Eq. (5)) of the heat source. Modeling the heat source was accomplished by implementation of Goldak's volumetric heat source in the ABAQUS [22] user-subroutine DFLUX.

$$q_f(x,y,z,t) = \frac{6\sqrt{3}f_fQ}{ab_fc\pi\sqrt{\pi}} e^{\frac{-3x^2}{a^2}} e^{\frac{-3[y-vt-y_0]^2}{b_f^2}} e^{\frac{-3z^2}{c^2}}, y \geq 0 \tag{4}$$

$$q_r(x,y,z,t) = \frac{6\sqrt{3}f_rQ}{ab_rc\pi\sqrt{\pi}} e^{\frac{-3x^2}{a^2}} e^{\frac{-3[y-vt-y_0]^2}{b_r^2}} e^{\frac{-3z^2}{c^2}}, y < 0 \tag{5}$$

a, b_f b_r and c are Goldak's weld pool characteristics. f_f and f_r, are fractions of heat deposited in front and rear half of the heat source, respectively. Q is heat source power calculated based on welding current and voltage as well as welding efficiency coefficient which was considered 0.85 in this study. Goldak's parameters should be calibrated so that nodal temperatures from simulation are verifiable by experimental measurements and dimensions of weld pool from simulation and macrograph section of the welded specimen reach favorable agreement. The heat source parameters and their values which were adjusted via iteration and applied for all simulation cases, are presented in the Table 6.

Thermal boundary conditions were set to model the heat loss during welding from free surfaces of the specimen via convection and radiation based on Newton's law of cooling and Stefan-Boltzmann's law, respectively. To consider combined effect of convection and radiation, two empirical formulae as presented in Eq. (6) were implemented in the ABAQUS user-subroutine FILM as practiced by other researchers [23,24].

$$h = \begin{cases} 0.0668 \times T & \left(\frac{W}{m^{2\circ}C}\right) 0 \leqslant T \leqslant 500 \\ 0.231 \times T - 82.1 & \left(\frac{W}{m^{2\circ}C}\right) T \geqslant 500 \end{cases} \tag{6}$$

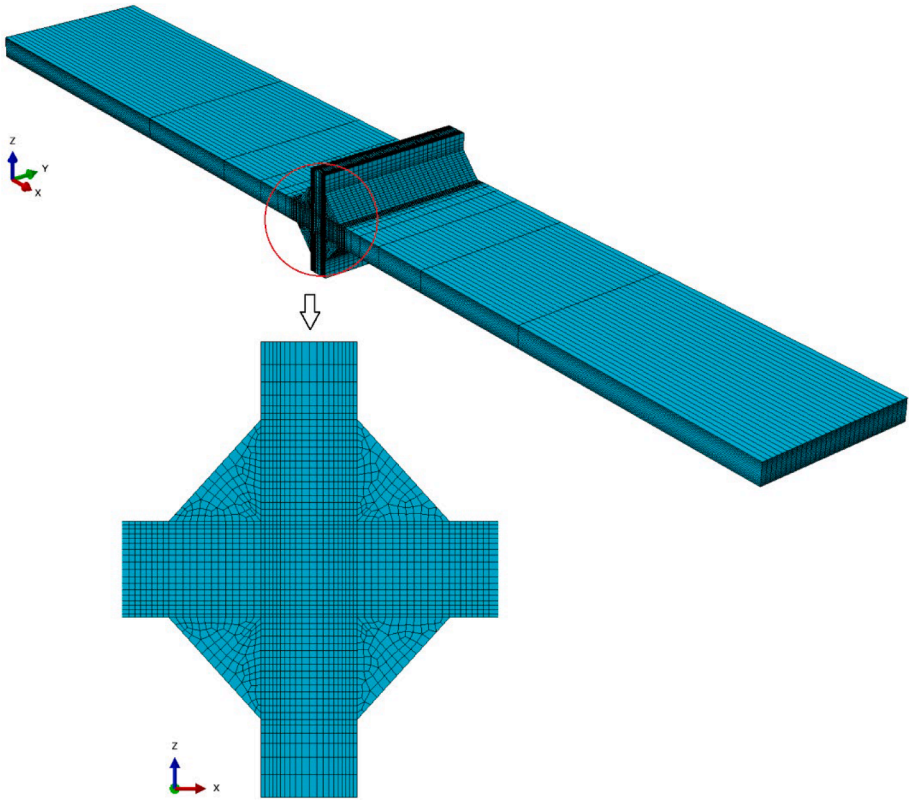

Fig. 6. FE mesh used in the thermal simulation.

Table 7
Material models used in FE-calculations.

Zone	$f_{y,FEM}$ [MPa]	E_t [MPa]	E [GPa]	ν [-]	ε_D	u_f	D_{max}
BM	1066	5604	200	0.3	0.0296	1	0.9
HAZ	709	6699	200	0.3	0.044	1	0.3
WM	968	9006	200	0.3	0.0296	1	0.9

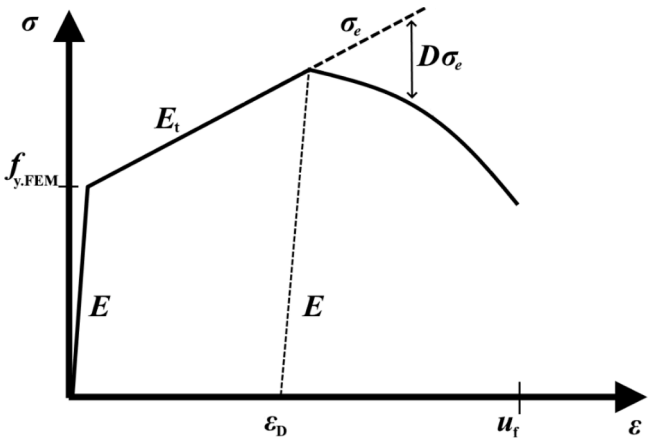

Fig. 7. Schematic presentation of the used material model.

where h denotes temperature dependent heat transfer coefficient.

Temperature dependent thermo-physical properties of base and filler materials required for solving the Eq. (3) were taken from the literature [25]. Three-dimensional models in this respect were developed and sequential addition of filler material was considered using element activation technique in ABAQUS. An 8-node linear heat transfer brick element (DC3D8) was used with temperature as the only degree of freedom at each node. The FE mesh used for the X-joint with 8 mm thickness is shown in Fig. 6. The interested reader is referred to the reference [26] for detailed information and considerations regarding thermal analysis and welding simulation of fillet welded joints.

2.3. Numerical strength calculations

In the FE analysis BM, WM, and HAZ were modeled using separate bi-linear constitutive models with an Abaqus damage evolution model. The used parameters are presented in Table 7 and a schematic presentation of the constitutive behavior is shown in Fig. 7. In the model, $f_{y,FEM}$ is the yield strength, ε_D is equivalent plastic strain at damage initiation, and D is the damage parameter. Since the value of effective plastic strain depends on the gauge length, in FE-modeling mesh size, Abaqus has the option of using the equivalent plastic displacement at fracture u_f to evaluate the damage.

The parameters for the material model were calibrated based on the experimental tensile test. First approximations of material models were generated using values from the material certificates and hardness measurement results. After each round of analysis, the values of the parameters were adjusted. The purpose of this procedure was to generate a model that could adequately reproduce the force–displacement curves obtained from the experiments up to ultimate tensile strength. A satisfactory match was achieved, as can be seen in the Experimental results section.

The authors acknowledge that the mesh size will influence the results. Because this paper aimed to study the effect of different degrees of geometrical and metallurgical constraint, only the stated mesh size was used. This is justified because the aim is not to generate an accurate assessment of ultimate capacity for the given joints, but to represent th effect of constraints.

The material model used and described above is based on the same justification. This model can reproduce the experimental results with reasonable approximation as shown in the experimental results section. In addition, the same model is used in all the calculations, which ensures that the relative effect of constraints can be presented and compared.

The authors acknowledge that the mesh size will influence the results. Because this paper aimed to study the effect of different degrees of geometrical and metallurgical constraint, only the stated mesh size was used. This is justified because the aim is not to generate an accurate assessment of ultimate capacity for the given joints, but to represent the effect of constraints.

The material model used and described above is based on the same justification. This model can reproduce the experimental results with reasonable approximation as shown in the experimental results section. In addition, the same model is used in all the calculations, which ensures that the relative effect of constraints can be presented and compared.

The geometry and mesh of FE models with the geometry parameters used in the present study are presented in Fig. 8 (a) and (b), respectively. Hereafter BF, XF, and AF are used as abbreviations for butt weld, X-joint, and arrow plate models, respectively. The models were generated and analyzed using commercial FE-software Abaqus CAE 6.14. Linear brick elements with reduced integration were used, with mesh size of approximately 1 mm. The length in the longitudinal direction of the models is 100 mm.

Symmetry was utilized at the YZ-plane in all models. In addition, XZ-plane symmetry was used in XF models. XY symmetry was not used because Björk et al., [27] noted that if a failure occurs at base material, the failure plane is at a 30° angle with respect to the tensile loading. The same behavior was noted in this study and is presented in the Results

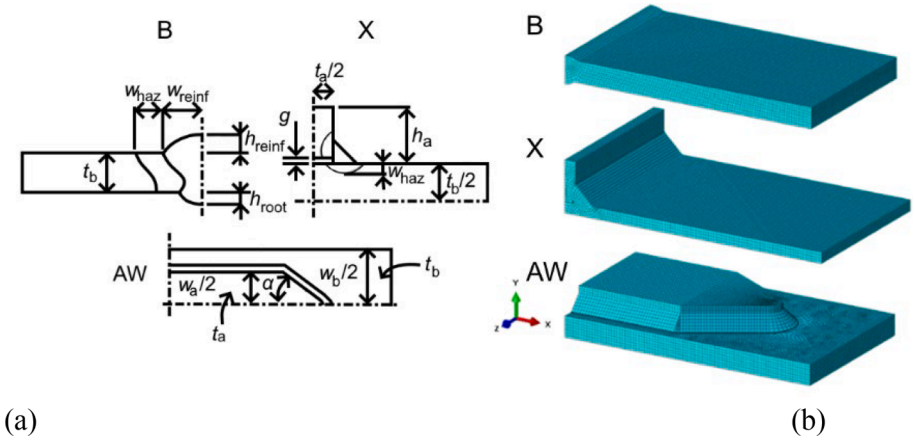

Fig. 8. Schematic presentation of parameters and figures of the generated FE-models.

Table 8
Geometry parameters used in FE-calculations.

Variable parameters							Constant parameters	
Butt weld							w_{reinf} [mm]	11
t_b [mm]	4	6	**8**	10			h_{reinf} [mm]	1.28
w_{haz} [mm]	1.5	3.0	**4.5**	6.0	7.5	9.0	h_{root} [mm]	1.4
X-joint								
t_a [mm]	**8**	16					a [mm]	5
t_b [mm]	6	**8**	10	12			g [mm]	0.1
w_{haz} [mm]	**2**	3.5	6.5				h_a [mm]	15
Arrow plate							t_a [mm]	8
α [°]	**60**	90	135	180			w_a [mm]	40
t_b [mm]	6	**8**	10	12			w_b [mm]	60

section. Loading was modeled using the forced displacement function attached to the nodes at the end of the base plate in a positive X-direction.

The test matrix for numerical calculations describing the used values for given parameters is presented in Table 8. In the table, constant parameters a and g denote throat thickness and the air gap in the X-joint respectively. The parameters corresponding to the experimental specimens are highlighted in the table.

The authors acknowledge that the mesh size will influence the results. Because this paper aimed to study the effect of different degrees of geometrical and metallurgical constraint, only the stated mesh size was used. This is justified because the aim is not to generate an accurate assessment of ultimate capacity for the given joints, but to represent the effect of constraints.

The material model used and described above is based on the same justification. This model can reproduce the experimental results with reasonable approximation as shown in the experimental results section. In addition, the same model is used in all the calculations, which ensures that the relative effect of constraints can be presented and compared.

3. Experimental results

The engineering stress–strain curves of as-received and as-welded specimens made from S960MC are shown in Fig. 9. As can be seen in Fig. 9, As-welded specimen shows significant strength reduction compared to the as-received specimen. Failure happened in the HAZ of the as-welded specimen, which was resulted from the HAZ softening attributed to the welded joints made from S960MC.

The load–displacement curves of all specimens are shown in Figs. 10-12 in which the solid lines illustrate the experimental tensile test results, and dashed lines represent the FE calculations. The numerical results can adequately represent the force–displacement behavior, up to ultimate tensile strength, observed in the tensile test. In the butt weld and X-joint, shown in Fig. 10 and Fig. 11, respectively, removing the constraint lowers the ultimate loading capacity. Removing the arrow plate did not affect the loading capacity (see Fig. 12). In all cases, the ultimate

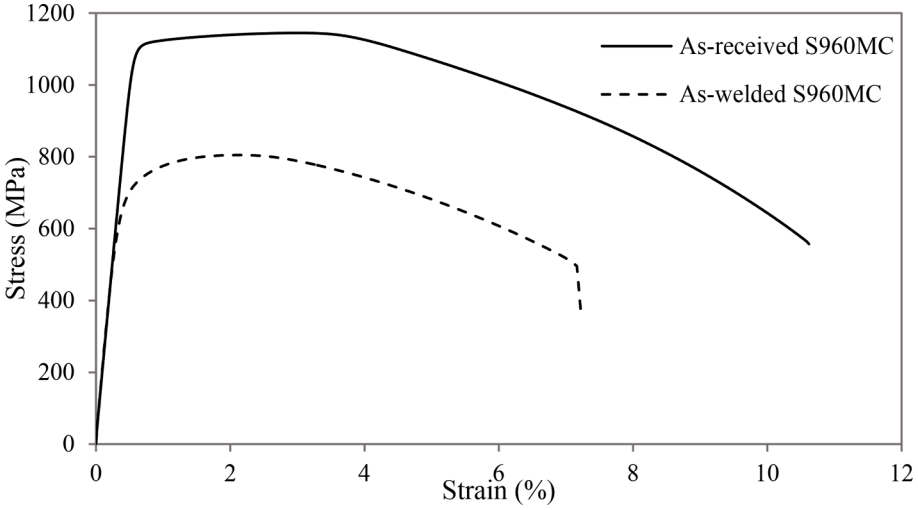

Fig. 9. Full range stress–strain curves for as-received and as-welded specimens made from S960MC.

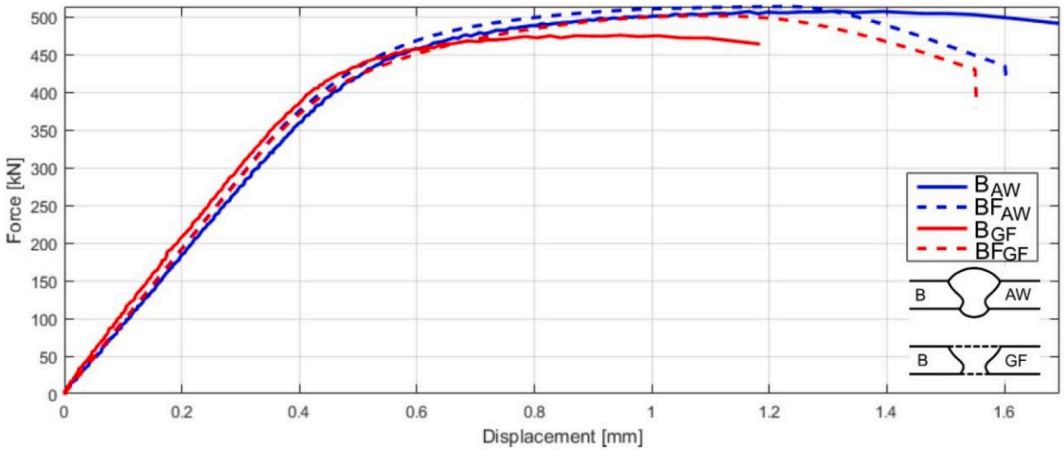

Fig. 10. Comparison between experimental butt weld specimens and FE-calculations.

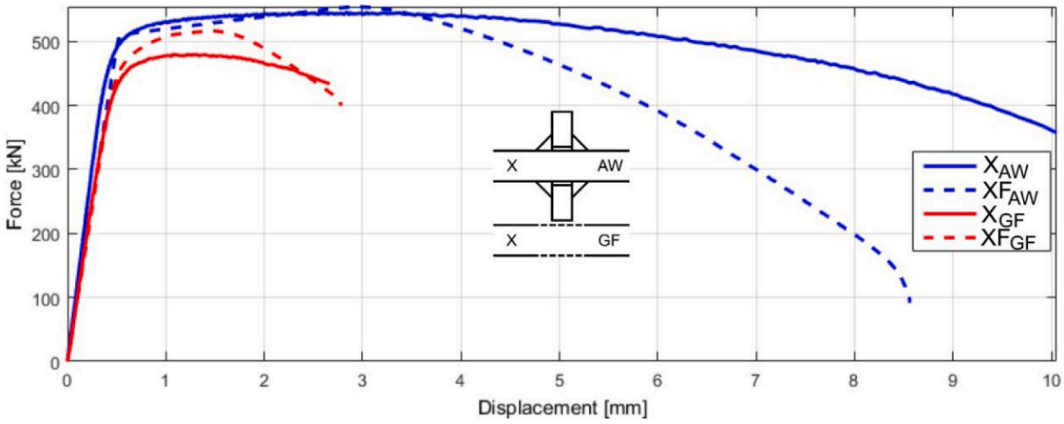

Fig. 11. Comparison between experimental X-joint specimens and FE-calculations.

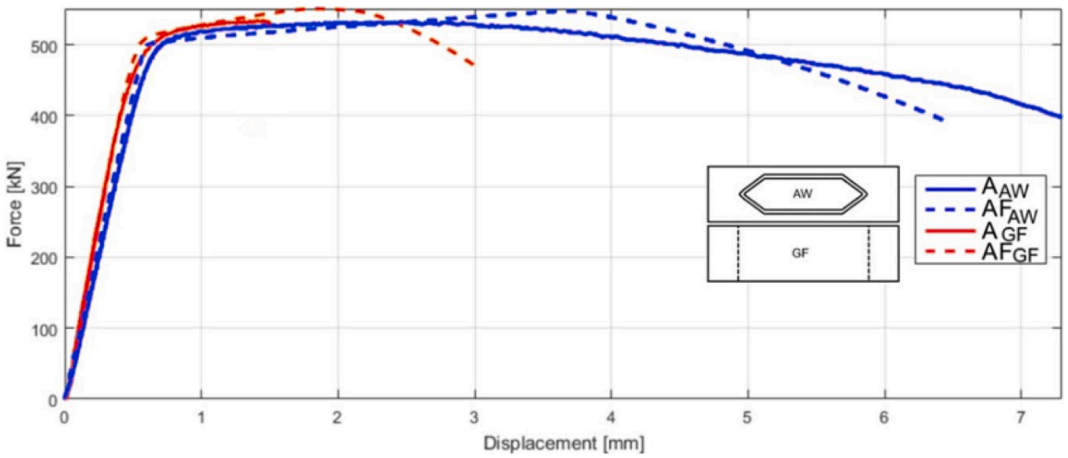

Fig. 12. Comparison between experimental arrow plate specimens and FE-calculations.

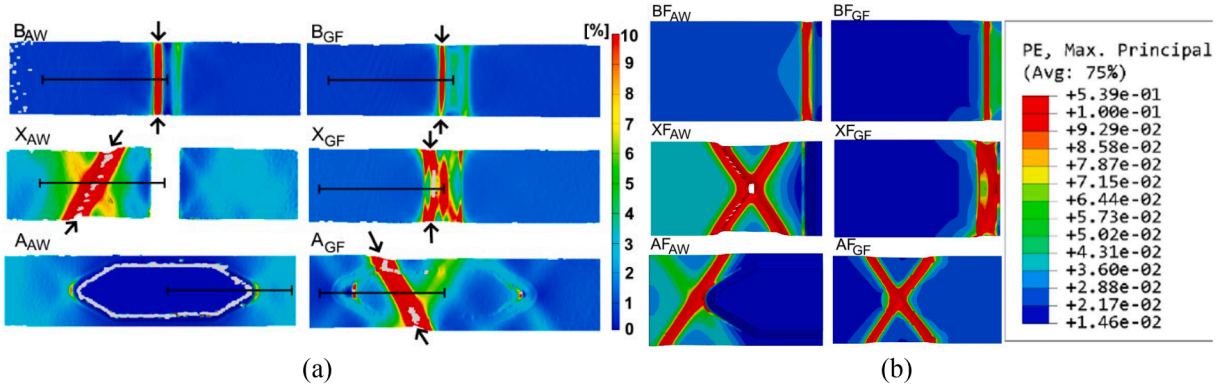

Fig. 13. Comparison of maximum principal strain fields between experimental results obtained using DIC (a) and numerical results (b).

elongation capacity is decreased due to the removal of the constraint.

The maximum principal strain contours from the DIC measurements and FE calculations are presented in Fig. 13 (a) and (b), respectively. The black arrows show the fracture location and direction. There is no black arrow indicating the fracture location of specimen A_{AW} because the fracture occurred outside the DIC measurement area as also shown in Fig. 13. Specimens X_{AW} and A_{AW} fractured from the base material at a 30° angle, which is consistent with the study performed by Björk et al., [27]. Furthermore, specimen A_{GF} fractured at a 30° angle, but in this case the fracture was affected by the HAZ.

Fig. 13 shows that the strain localization occurs in the same relative position in specimens B and BF, and X and XF. In both set B specimens, the strain localization and the fracture occurred in the softened HAZ. Specimen X_{GF} fractured from the soft HAZ region. In specimen AF_{AW}, the strain localized to the base material as in A_{AW}, which was not the case for specimen AF_{GF}. In A_{GF}, the strain localization occurred in the place where the arrow plate located prior machining. In the numerical model, the strain was localized at the tip of the removed arrow plate. The fracture surfaces of the specimens are presented in Fig. 14. A typical ductile fracture surface can be observed in all specimens.

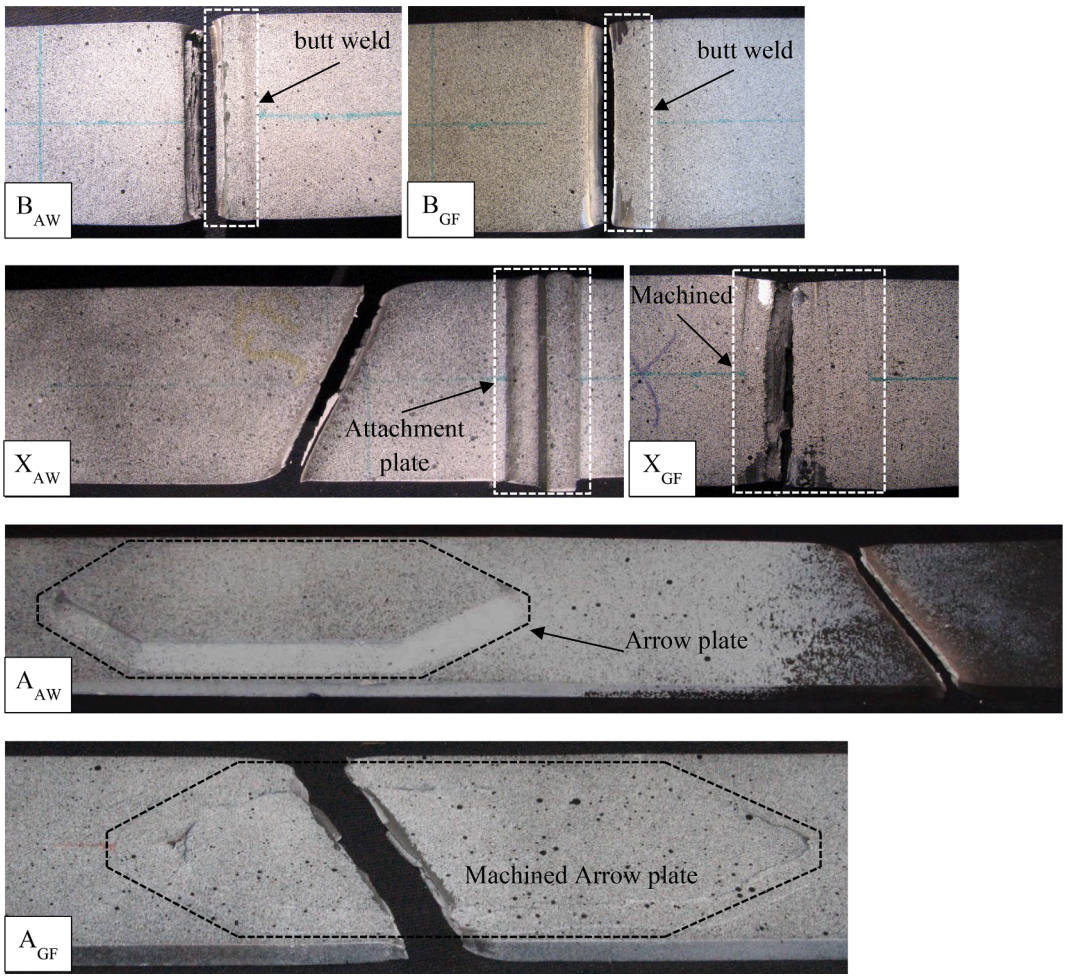

Fig. 14. Top view of the fractured specimens with different failure locations.

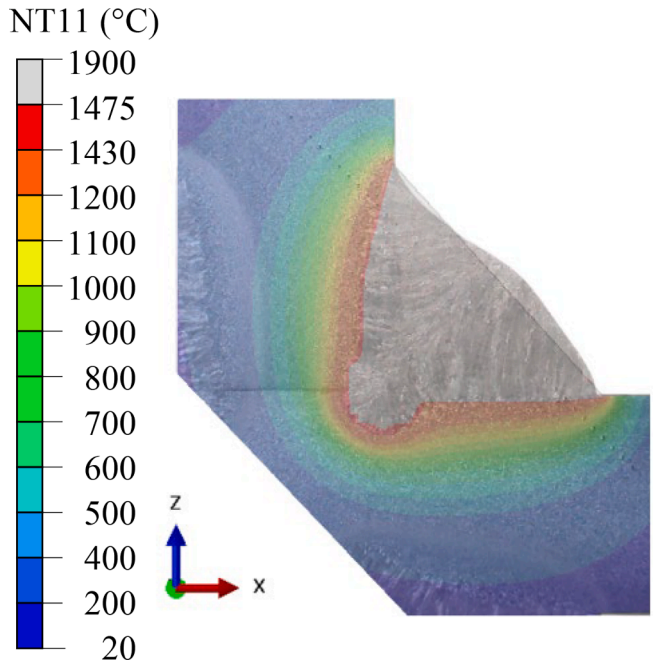

Fig. 15. Welding temperatures and boundaries of fusion zone from simulation and weld macrograph.

4. Results from numerical calculations

4.1. Thermal analysis

Accurate prediction of the temperature histories during the welding requires calibration of the thermal model. correct prediction of the weld pool geometries is one of the measures to show the correctness of the thermal analysis. In this regard, the results of simulation were evaluated against the macrograph of the polished weld cross section for the 8 mm thick X-joints, as shown in Fig. 15.

As shown in Fig. 15, numerical results in terms of boundaries of the fusion zone such as the depth and width of penetration are in good agreement with the experimental macrograph, which indicates the temperature histories have been predicted correctly. Based on the calibration of the thermal model for the 8 mm thick X-joint, for the sake of comparison, simulations for the similar joints and welding parameters, albeit with different thicknesses, i.e., 6 and 10 mm were performed. Thermal contours and welding temperatures in the mid-section of each simulation case during the welding are depicted in Fig. 16.

As it was shown in Fig. 3, a reduction in hardness was clearly present at the SCHAZ. In this regard, the maximum temperature in this region plays an important role. Based on the temperature history, the highest reduction in the hardness was present at regions reaching a maximum temperature of 750–920 °C, see Fig. 17(a). In maximum temperatures of 750 °C and below, the hardness gradually increases again and reaches BM hardness at the maximum temperature of 500 °C. Based on the procedure, the hardness distributions are estimated for the plate thickness with simulated temperature histories (t = 6 mm, 8 mm, and 10

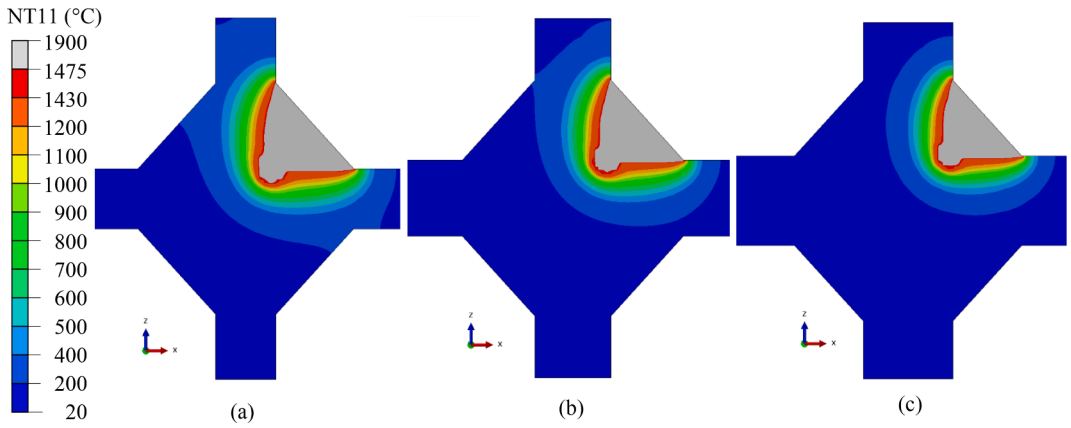

Fig. 16. Temperature distribution during the welding of the first pass at mid-section for (a) thickness 6 mm, (b) thickness 8 mm, and (c) thickness 10 mm.

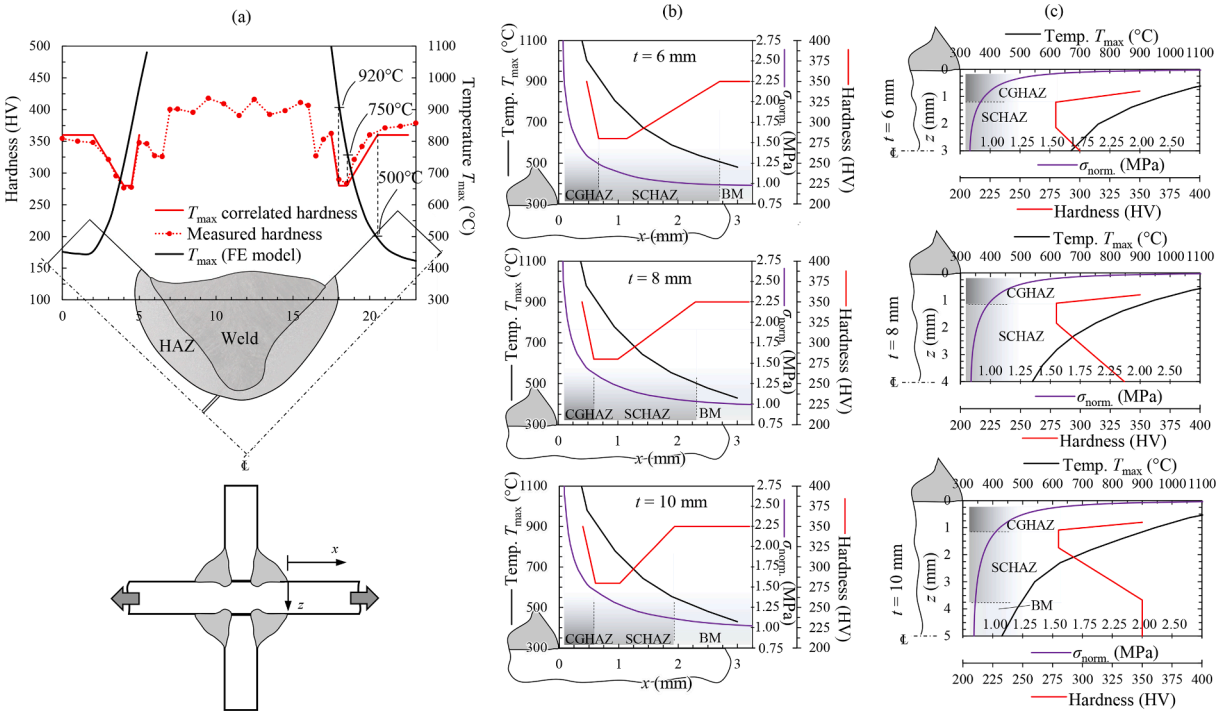

Fig. 17. (a) Approximated model for the hardness based on the maximum temperature for the plate thickness of t = 8 mm, and notch stress distributions and numerically obtained strength (b) in the through-thickness direction and (c) at the plate surface for the different plate thicknesses (t = 6 mm, 8 mm, and 10 mm).

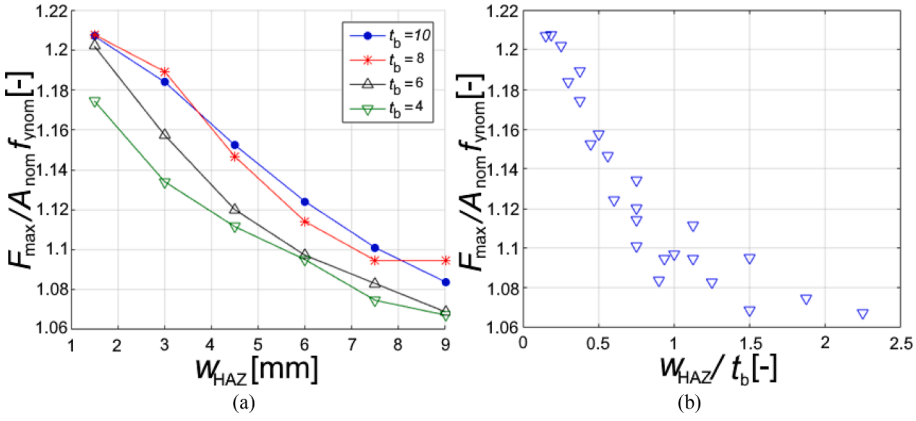

Fig. 18. Relative ultimate loading capacities of FE-analyzed butt joints with different (a) HAZ widths and (b) HAZ to plate thickness ratios.

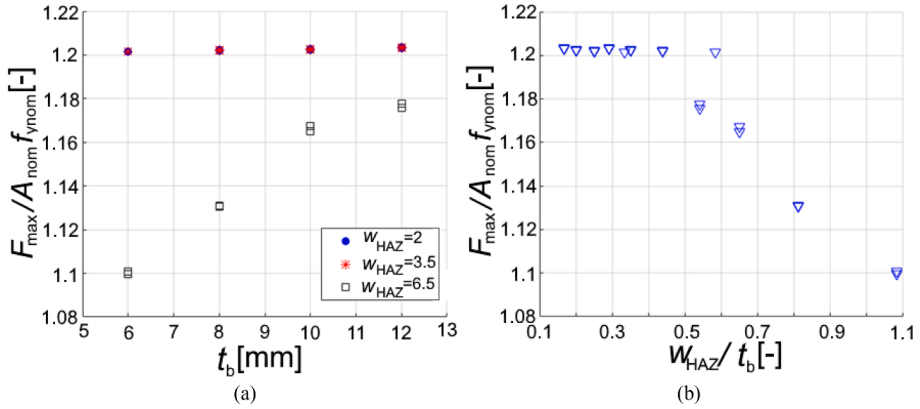

Fig. 19. Relative ultimate loading capacities of FE-analyzed X-joints with different (a) plate thicknesses and (b) HAZ to plate thickness ratios.

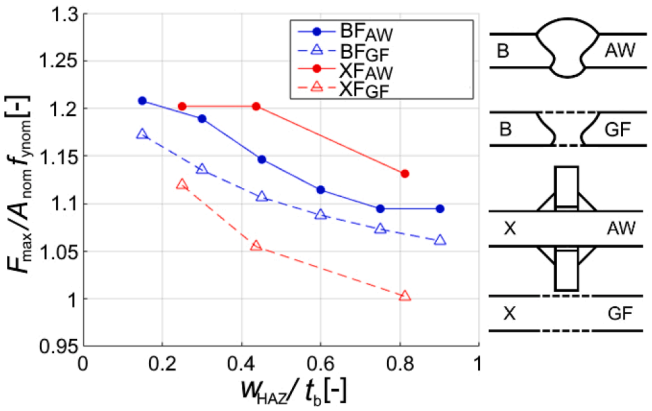

Fig. 20. Effect of geometrical constraint on the relative ultimate load-carrying capacity of the specimens BF and XF.

mm), considering distributions in both plate surface (x) and thickness (z) directions, see Fig. 17 (b–c). In addition, to investigate the constraint effect with respect to the material softening, normalized normal stress ($\sigma_{norm.}$) distributions, transverse to the fillet weld, were obtained for all plate thicknesses.

Due to the notch stress caused by the weld toe transition, the plane stress condition changes into the plane strain condition in the vicinity of the weld, inducing triaxial stress state. With the thinner plates, the softening occurs beyond this area as the normalized stress reaches the region with $\sigma_{norm.} = 1$ MPa. The results also indicate that the size of zone experiencing 750 °C–920 °C maximum temperature does not significantly enlarge with smaller plate thickness but, instead, the reduced hardness can be found further from the weld toe, as shown by the shallower slopes in Fig. 17(b). Furthermore, in the in-depth (z) direction Fig. 17(c), softening occurs in the whole cross-section with the thickness of $t = 6$ mm while with the plate thickness of $t = 10$ mm only into the depth of 3–4 mm from the plate surface. A more detailed analysis on the strength capacity with different HAZ widths is carried out in Section 4.2.

4.2. Strength analysis

The effect of the width of the HAZ on ultimate loading capacity was studied, using the parametrical models of BF_{AW}. The results of these FE analyses are presented in Fig. 18. The results indicate that as the width of the HAZ increases irrespective of the thickness of the base plate, the ultimate loading capacity of the joint is reduced as the value of w_{HAZ}/t_b increases.

The results of parametrical models of XF_{AW} are presented in Fig. 19. Base plate thickness had no effect on the ultimate capacity of the models with HAZ widths of 2 mm and 3.5 mm, as shown in Fig. 19 (a). Fig. 19 (b) indicates that as the value w_{HAZ}/t_b is higher than 0.5, the ultimate loading capacity of the joint is reduced.

The results presented above included both the geometric constraint caused by the weld beat and the attached plate and the metallurgical constraint generated by strength mismatch between adjacent materials. Fig. 20 presents the effect of geometric constraint in specimens BF and XF with different w_{HAZ}/t_b ratios. According to the results, the geometric constraint increases the ultimate load-carrying capacity by approximately 5% in butt joint specimens and approximately 10% in X-joint specimens, compared to when only a metallurgical constraint is present in the weldment.

Numerical calculations seem to indicate that both the angle of the arrow plate and the thickness of the base plate have only a minor effect

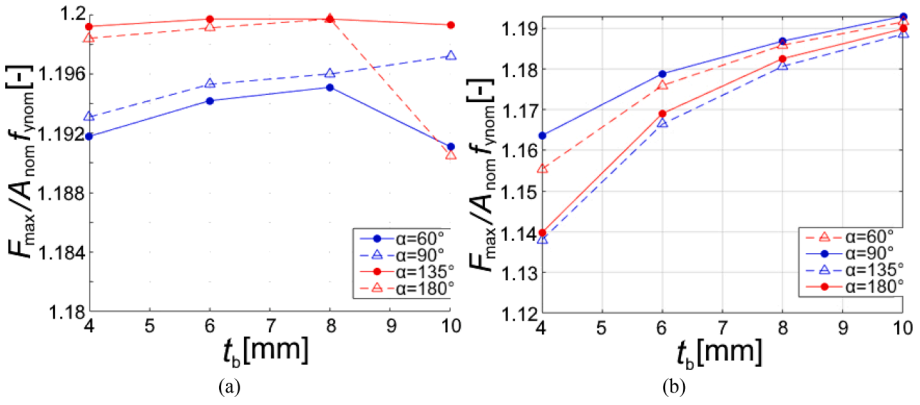

Fig. 21. AP model ultimate loading capacities with (a) and without constraint (b).

on the ultimate loading capacity of the joint (see Fig. 21 (a)). Fig. 21 (b) presents the results from the model with the constraint removed. As can be seen, the geometric constraint caused by the arrow plate is minimal. In the worst case, the relative ultimate capacity without the constraint is 1.14. and with constraint caused by the arrow plate is 1.19. On the other hand, removing the arrow plate has a major effect on the ultimate elongation capacity of the specimen, as shown in Fig. 12.

5. Discussion

The results obtained from the laboratory tests and FEA models in the butt welded specimens are similar to those reported in previous studies [10-14]. The change of w_{HAZ}/t_b is attributed to the welding heat input which can also be associated with the welding process as well, i.e. laser welding and GMAW. The previous studies in the literature only consider certain heat input values, joint type, or welding process [28,29,30]. However, the current research is generalized to provide a broader overview of the phenomena for practical applications. The results show that the ultimate load-carrying capacity of the joint decreases as the ratio w_{HAZ}/t_b increases in butt welded specimens. However, the numerical results from X-joints seem to indicate that HAZ dimensions must reach a certain threshold value before the detrimental effect can be observed. When the cut-off value is exceeded, the X-joint seems to obey the same principle as the butt welded joint, namely that the ultimate load-carrying capacity decreases as the w_{HAZ}/t_b increases.

In experimental tests and FE analyses, the effect of the geometric constraint was studied by removing the weld beads and attached plates by machining and not including them in the numerical models, respectively. In the experimental tensile test of the arrow plate specimens, the geometric constraint had no notable effect on the ultimate load-carrying capacity, even though the failure location shifted from the base plate to the place where the arrow plate was attached prior to machining. This was somewhat unexpected because the failure location included the softened HAZ in the latter case. On the other hand, the soft zone in the arrow plate specimens was small compared to the dimensions of the base plate.

The effect of the geometric constraint on the butt welded experimental and numerical specimens was small compared to that on the X-joint and arrow plate specimens with small base plate thickness. This was comprehensible because in the butt welded specimen, only the weld bead forms the geometric constraint, whilst in the X-joint and arrow plate, both the weld bead and the attached plate generate the constraint. According to the numerical results, the strengthening effect is approximately 5% regardless of the w_{HAZ}/t_b ratio in the studied cases. In the case of the X-joint, the geometric constraint was responsible for an increase of approximately 10% in the ultimate load-carrying capacity compared to situations without the constraint.

According to the experimental results, removing the geometric constraint had a detrimental effect on the deformation capacity of the weldments. This effect was more profound than the effect on the ultimate load-carrying capacity. It appears that the geometric constraint prevents the strain from localizing to the softened HAZ. Neuvonen et al., [15] showed that it is possible to assess the elongation capacity of weldments when there is sufficient information about material properties. The models used in the current study were not suitable for further investigations concerning the elongation capacity.

In this study, the material models were created based on the hardness measurements and material certificates. The values obtained from these sources were slightly modified to achieve suitable agreement between the experimental and numerical results. The hardness-based estimation for the yield strength of the BM (see Table 5) seemed to be slightly conservative compared to the values of the material certificate and tensile test (see Table 2 and Fig. 9.). However, for the HAZ, the corresponding values were not available but still a reasonable agreement with the experimentally and numerically obtained ultimate capacities were obtained (see Figs. 10–12). Further research should, however, shed light on the validity of Equations (1)–(2) for estimating the material properties at BM, WM and HAZ.

The results indicate that by properly designing weldments, it is possible to utilize the geometric constraint effect to shift the failure to the base material, and thus prevent making the weak soft region in the HAZ act as the weakest link in the joint. In so doing, it is possible to create weldments with good mechanical properties.

In addition, it seems that to gain more knowledge regarding the effects of geometric and metallurgical constraints on the ultimate capacity of welded joints, advancements must be achieved in tensile testing and interpretation of results, as well as in the material parameters of the identification process. Before such knowledge is gained, researchers and design engineers must acknowledge that these effects are present and that in suitable circumstances, the effects of the constraints should not be neglected.

Special consideration must be given to the butt welds of thin plates, because the w_{HAZ}/t_b ratio in these cases might be high. A common workshop method is to use heat treatment to straighten plate structures after welding. This might generate a soft HAZ without geometric constraints and thus cause a decrease in the ultimate loading and elongation capacity of the structure.

6. Conclusions

The most important finding of this study is that geometric constraints can have a positive effect on the ultimate capacity of weldments manufactured from DQ UHSS. Without the constraint effect in welds with a relatively wide softened zone due to welding, both the ultimate load-carrying capacity and elongation capacity can be lower than the corresponding properties of the base material, at least in the studied joint types.

The results indicate that in the butt weld specimens, the load-carrying capacity decreases as the HAZ width increases. On the other hand, the X-joint seems to possess a threshold value for relative HAZ width, and when the specific value is exceeded, the increase in HAZ width decreases the ultimate load-carrying capacity by shifting the fracture from the base material to the HAZ. When the threshold value of the relative HAZ width is not exceeded, the HAZ width does not have a notable effect on the ultimate load-carrying capacity of the X-joint and the failure occurs at the base material.

This study shows that in addition to the narrow HAZ, the geometry of the joint must also be considered. By designing weldments with enough rigid geometric constraints, compared to the width of the softened zone, the susceptibility to softening of DQ UHSS can be managed, and the capacity of the base material fully utilized. Utilizing this approach could help humankind reduce the amount of steel used and thus aid in lowering the environmental effect of the steel industry.

Declaration of Competing Interest

The authors declare that they have no known competing financial interests or personal relationships that could have appeared to influence the work reported in this paper.

Acknowledgements

The authors would like to thank DIMECC Ltd, Business Finland (previously TEKES), SSAB AB and all participants in the “Breakthrough Steels and Applications” (BSA) and “Fossil-Free Steel Applications” (FOSSA) research programs.

References

[1] Aksel H, Eren Ö. A discussion on the advantages of steel structures in the context of sustainable construction. Int J Contemp Archit 2015;2(3):46–53.

[2] Kömi J, Karjalainen P, Porter D. "Direct-quenched structural steels," in Encyclopedia of Iron. In: Colás R, Totten GE, editors. Encyclopedia of Iron, Steel, and Their Alloys. CRC Press; 2016. p. 1109–25.
[3] Muckelroy NC, Findley KO, Bodnar RL. Microstructure and mechanical properties of direct quenched versus conventional reaustenitized and quenched plate. J Mater Eng Perform 2013;22(2):512–22.
[4] Meysami AH, Ghasemzadeh R, Seyedein HS, Aboutalebi MR. An investigation on the microstructure and mechanical properties of direct-quenched and tempered AISI 4140 steel. Mater Des 2010;31(3):1570–5.
[5] Chang W-S. Microstructure and mechanical properties of 780 MPa high strength steels produced by direct-quenching and tempering process. J Material Sci 2002;37 (10):1973–9.
[6] E. c. f. standardization, "Eurocode 3 - Design of steel structures - Part 1-12: Additional rules for the extension of EN 1993 up to steel grades S 700," 2007.
[7] E. C. f. standardization,. Cranes - Mobile cranes 2014.
[8] D. A. Porter, "Weldable High-Strength Steels: Challenges and Engineering Applications," in IIW International Conference High-Strength Materials - Challenges and Applications, Helsinki, 2015.
[9] Skriko T. Dependence on Manufacturing Parameters on the Performance Quality of Welded Joints Made of Direct Quenched Ultra-High.Strength Steel. Lappeenranta: Acta Universitatis Lappeenrantaensis; 2018.
[10] Björk T, Ahola A, Tuominen N. On the design of fillet welds made of ultra-high-strength steel. Welding in the World 2018;62(5):985–95.
[11] Amraei M, Skriko T, Björk T, Zhao X-L. Plastic strain characteristics of butt-welded ultra-high strength steel (UHSS). Thin-Walled Struct 2016;109:227–41.
[12] Ran M-M, Sun F-F, Li G-Q, Kanvinde A, Wang Y-B, Xiao RY. Experimental study on the behavior of mismatched butt welded joints of high strength steel. J Constr Steel Res 2019;153:196–208.
[13] Rodrigues DM, Menezes LF, Loureiro A, Fernandes JV. Numerical study of the plastic behaviour in tension of welds in high strength steels. Int J Plast 2004;20(1): 1–18.
[14] Sun F-F, Ran M-M, Li G-Q, Kanvinde A, Wang Y-B, Xiao RY. Strength model for mismatched butt welded joints of high strength steel. J Constr Steel Res 2018;150: 514–27.
[15] Neuvonen R, Skirko T, Björk T. Use of the quasi-static johnson-cook model in the failure assasement of tensile specimens with metallurgical constraints. Eur J Mech A Solids 2020;82.
[16] SFS-EN 1011-2. Welding. Recommendations for welding of metallic materials. Part 2: Arc welding of ferritic steels, Helsinki, 2001.
[17] Standard Test Methods for Tension Testing of Metallic Materials ASTM E8 / E8M, Conshohocken: American Society for Testing and Materials, 2013.
[18] Ghafouri M, Amraei M, Pokka A-P, Björk T, Larkiola J, Piili H, et al. Mechanical properties of butt-welded ultra-high strength steels at elevated temperatures. J Constr Steel Res 2022;198:107499.
[19] Amraei M, Afkhami S, Javaheri V, Larkiola J, Skriko T, Björk T, et al. Mechanical properties and microstructural evaluation of the heat-affected zone in ultra-high strength steels. Thin-Walled Struct 2020;157:107072.
[20] Pavlina EJ, Van Tyne CJ. Correlation of yield strength and tensile strengthwith hardness for steels. J Mater Eng Perform 2008;6(17):888–93.
[21] Goldak J, Chakravarti A, Bibby M. A new finite element model for welding heat sources. Metall Trans B 1984;15(2):299–305.
[22] ABAQUS user's manual, Version 2020., Dassault Systèmes®, 2020.
[23] Ghafouri M, Ahola A, Ahn J, Björk T. Numerical and experimental investigations on the welding residual stresses and distortions of the short fillet welds in high strength steel plates. Eng Struct 2022;260:114269.
[24] Yaghi A, Hyde T, Becker A, Sun W, Williams J. Residual stress simulation in thin and thick-walled stainless steel pipe welds including pipe diameter effects. Int J Press Vessel Pip 2006;83(11–12):864–74.
[25] Ghafouri M, Ahn J, Mourujärvi J, Björk T, Larkiola J. Finite element simulation of welding distortions in ultra-high strength steel S960 MC including comprehensive thermal and solid-state phase transformation models. Eng Struct 2020;219:110804.
[26] Ghafouri M, Ahola A, Ahn J, Björk T. Welding-induced stresses and distortion in high-strength steel T-joints: numerical and experimental study. J Constr Steel Res 2022;189:107088.
[27] Björk T, Nykänen T, Valkonen I. On the critical plane of axially loaded plate structures made of ultra-high strength steel. IIW-Document XV-1492-15.;18:p., 2015.
[28] Lan X, Chan T-M, Young B. Structural behaviour and design of chord plastification in high strength steel CHS X-joints. Constr Build Mater 2018;191:1252–67.
[29] Guo W, Li L, Dong S, Crowther D, Thompson A. Comparison of microstructure and mechanical properties of ultra-narrow gap laser and gas-metal-arc welded S960 high strength steel. Opt Lasers Eng 2017;91:1–15.
[30] Liu X, Chung K-F, Ho H-C, Xiao M, Hou Z-X, Nethercot DA. Mechanical behavior of high strength S690-QT steel welded sections with various heat input energy. Eng Struct 2018;175:245–56.